



A comparative study on 2D and 3D magnetic field analysis of permanent magnet synchronous motor using FEM simulations

Maria C. Pechlivanidou, Ioannis D. Chasiotis and Yannis L. Karnavas 

Electrical Machines Laboratory, Department of Electrical & Computer Engineering, Democritus University of Thrace, Xanthi, Hellas (GR), Greece

ABSTRACT

Permanent magnet synchronous motors (PMSMs) have recently gained increasing industrial and research interest. The PMSM design and especially its performance evaluation through two-dimensional (2D) and three-dimensional (3D) magnetic field analysis using finite element method (FEM) is not trivial, as it is a quite demanding and time consuming procedure. Furthermore, there has always been doubt on the accuracy of 2D analysis results and on which type of analysis is the most preferable one for the specific motor. This work aims to emphasize the difficulties and the advantages that arise from the 3D analysis. The aforementioned simulations were performed for the case of a four-pole PMSM. Several magnetic and electromechanical quantities have been determined. Additionally, various materials were utilized for the construction of stator and rotor cores and their effect on the motor's behavior was investigated. Finally, the derived results are compared and useful conclusions regarding the solution accuracy are given.

ARTICLE HISTORY

Received 25 October 2018

Accepted 24 September 2019

KEYWORDS

2D and 3D finite-element analysis; airgap flux density distribution; solution accuracy; surface-mounted magnets; permanent magnet synchronous motor

1. Introduction

Recent industrial trends and consumers' requirements impose the development of electrical motors with high efficiency, smaller size, longer operating life and relatively low operating and manufacturing costs [1]. Permanent magnet synchronous motors (PMSMs) with surface mounted magnets fulfil the aforementioned features, as they present the following characteristics and/or advantages over other types of electrical motors [2–5]: (a) high efficiency over a wider operating range, (b) smaller radial forces as a larger airgap length is applicable, (c) reliable performance and increased durability, (d) low temperature distribution during operation owing to the absence of rotor losses, (e) electrical stability, (f) high power/torque density and less weight, (g) satisfactory flux-weakening capability and higher continuous torque over a wider speed range, (h) enhanced dynamic performance under load due to lower rotor inertia and (i) facile manufacturing procedure. Therefore, there has been increasing research interest for this topology and its application field range

CONTACT Yannis L. Karnavas  karnavas@ee.duth.gr  Electrical Machines Laboratory, Department of Electrical & Computer Engineering, Democritus University of Thrace, 671 00 Xanthi, Greece

is impressive, as PMSMs are used in numerous industrial, residential, agricultural, aerospace and military applications such as coolant pumps, compressors, air conditioning and lifting systems, washing machines, electric or hybrid passenger and public transportation vehicles, heavy-duty vehicles (excavators, armoured fighting vehicles, etc.) as well as aircraft and ship propulsion systems [6,7].

At the same time, and although the design process of PMSMs has been improved throughout the last decade mainly by the incorporation of efficient optimization techniques e.g. [8], there are still some factors which have remained critical to engineers. Among others, the accurate estimation of several motor's performance parameters is an essential step of the overall computer-aided design procedure. For this purpose, several approaches based on magnetic equivalent circuits have been developed [9]. Despite the fact that this methodology seems to lead to quite accurate results compared to experimental measurements, the adopted equivalent circuits and the mathematical equations that describe them exhibit increased complexity [10]. Thus, the two and three-dimensional (2D and 3D) magnetic field analysis of PMSMs using Finite-Element Method (FEM) can be considered as a very attractive alternative [11].

Electromagnetic problems of electrical machines are solved in 2D and 3D depending on the problem nature. Radial flux PMSMs are usually represented by two-dimensional models and in typical cases, the simulation is completed in a few minutes. Until nowadays, a large amount of 2D analytical methods with varying degree of accuracy has been proposed and incorporated in the design and performance analysis procedure [12]. However, PMSM topologies have often variations in the third dimension, which cannot be accurately taken into account in 2D models. For instance, a variation of this kind is provoked when skewed stator slots and/or skewed permanent magnets are used. In such cases, the conduction of 3D simulations is required, as stated in [13], in which the effect of skewed surface-mounted permanent magnets on the performance of a brushless DC motor has been studied. Furthermore, the solution which arose by 3D models has been proved more accurate compared to the corresponding one derived through 2D simulation. The analysis of the influence of the 2D and 3D meshes in the estimation of the eddy-current losses in PMSMs, which was conducted in [14], revealed that 2D time-dependent finite-element analysis concludes to satisfactory results. However, the solution accuracy is compromised if the axial length of the magnets is comparable to their other dimensions. On the other hand, the conduction of 3D analysis is very time consuming and requires significant computational resources [15]. In many cases, (i.e. when typical computers are used), the simulation of PMSMs takes from a half to a few days in order to be completed. Several techniques, such as multi-slice modelling and massive parallel computation, have been implemented in order to reduce sufficiently the size of the model while at the same time a relatively fast simulation is possible [16,17].

The best scenario for engineers is to conclude to a solution almost as fast as 2D and almost as accurate as 3D. As the above perspective is not feasible, it is essential to estimate the solution error arising from the classical 2D models and to determine which type of analysis is preferable, for PMSMs performance evaluation taking into account the specific problem requirements. A review in the relevant literature shows that similar research effort was conducted with respect to single and three-phase inductions motors mainly. Simulation results for the calculation of various motor's electrical parameters and the estimation of magnetic saturation and harmonics of airgap flux density distribution derived through

2D and 3D magnetic field analysis are reported e.g. in [18–21]. Moreover, in [22] it has been shown that the level of error resulting from the use of 2D analysis as compared to 3D analysis is not important and can be considered acceptable especially for small single-phase shaded pole induction motors.

However, the above conclusions and observations cannot be adopted in the case of PMSMs. The specific motor configuration differs significantly from one of induction motors, while at the same time some phenomena such as cogging torque are not observed in the latter case [23]. Also, the torque ripple, the magnetic saturation of rotor core steel and the slot opening effect are more common phenomena in PMSMs [24]. Thus, the accuracy of the 2D and 3D magnetic field analysis on PMSMs should be investigated more. Consequently, the determination of the airgap flux density distribution and its components (i.e. radial and circumferential flux density) are of great importance. The amplitude and the quality of this parameter affect remarkably several other magnetic and electromechanical quantities, such as the average output torque, the torque ripple, the flux density distribution over the different motor's parts and consequently the motor's performance [25,26].

Based on the above, the present study chose a typical four-pole PMSM with surface-mounted magnet as a reference in order to investigate and compare the accuracy of the results obtained through 2D and 3D magnetic field analysis. For this purpose, the airgap flux density has been considered as a comparison measure of the solution accuracy. The design specifications and the characteristics of the investigated topology are analytically presented in Section 2 whereas the theoretical and the mathematical background that governs PMSMs electromagnetic problems are also described. The derived results from 2D and 3D analysis are given in Section 3 and 4 respectively, while at the same time, the influence of the use of various ferromagnetic materials for the stator and rotor cores on motor's performance is investigated. Relevant discussion regarding the comparison of the results is made in Section 5 and some useful recommendations about which analysis type is more preferable for given computational resources are also provided. Finally, Section 6 summarizes and concludes the work.

2. Problem statement and relevant background

2.1. Description of the problem

A typical PMSM involves a balanced three-phase winding, whose coils are wound around stator's teeth, while permanent magnets are mounted on the rotor surface creating a constant magnetic field. The three-phase windings are excited by the currents which are described by,

$$\begin{aligned} I_a &= I_{peak} \cos(\omega t) \\ I_b &= I_{peak} \cos(\omega t + 120^\circ) \\ I_c &= I_{peak} \cos(\omega t - 120^\circ) \end{aligned} \quad (1)$$

The configuration adopted here is a four-pole, three-phase PMSM with inner rotor topology, which is supposed to be used in low-power applications. The stator consists of 24 slots featuring a full pitch distributed lap winding. Stator's core outer diameter is 120 mm, rotor's core outer diameter is 67 mm and motor's active length is 65 mm. The airgap length has

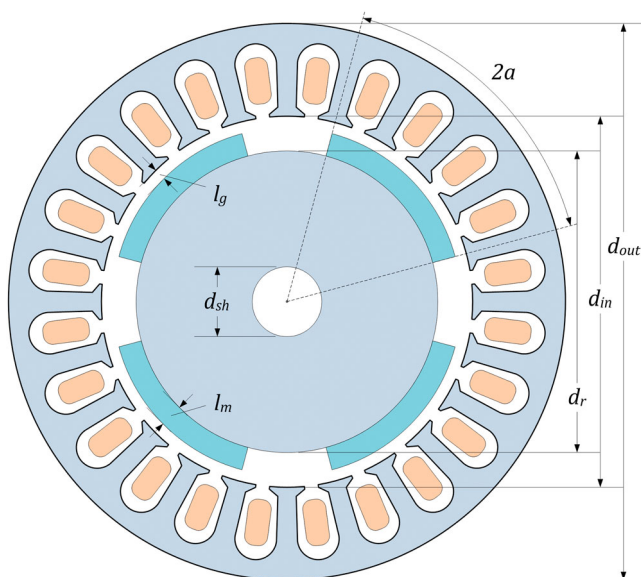


Figure 1. Cross section of the adopted PMSM's assembly.

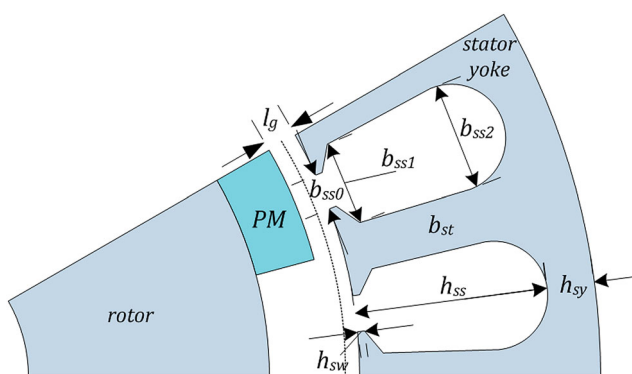


Figure 2. Detailed stator slots geometrical parameters of PMSM under study.

been selected to be equal to 0.5 mm. Figure 1 shows an overall cross section view of the examined PMSM, in which basic geometrical parameters are also depicted. Furthermore, a cross section of the motor with detailed geometrical characteristics of the stator slots is presented in Figure 2. The aforementioned quantities as well as motor's specifications are analytically given in Tables 1–3. The rotor consists of four neodymium type permanent magnets (NdFeB 35) which are alternately poled and magnetized radially (i.e. through their smaller dimension). The material used for these magnets exhibit high energy density and can tolerate up to 150°C operating temperature.

Regarding to the ferromagnetic material for the construction of rotor and stator cores, typical commercial electrical steels have been chosen in order to investigate their impact on motor's performance. The materials adopted here are the following (their commercial

Table 1. Specifications of the PMSM under study.

Quantity	Symbol	Value	Unit
Output power	P_{out}	550	W
Output torque	T_{out}	3.50	Nm
Synchronous speed	n_s	1500	rpm
Angular frequency	ω	188.50	rad/sec
Line to line voltage	V_{pp}	220	V
Electrical frequency	f	50	Hz
RMS phase current	I_{rms}	1.70	A
Peak phase current	I_{peak}	2.40	A

Table 2. PMSM's stator core and slots design variables.

Quantity	Symbol	Value	Unit
Stator core outer diameter	d_{out}	120	mm
Stator core inner diameter	d_{in}	75	mm
Stator core active length	L_{stat}	65	mm
No. of stator slots	q	24	–
Slot opening width	b_{ss0}	2.50	mm
Slot top width	b_{ss1}	5.60	mm
Slot base width	b_{ss2}	7.60	mm
Stator teeth width	b_{st}	4.70	mm
Stator slot height	h_{ss}	13.50	mm
Stator tooth tip height	h_{sw}	1.50	mm
Stator yoke height	h_{sy}	9.00	mm
No. of conductors/slot	N_N	58	–
Wire diameter	d_{cond}	0.9116	mm
Wire area	A_{cond}	0.6527	mm ²

Table 3. PMSM's rotor core and magnets' design variables.

Quantity	Symbol	Value	Unit
No. of permanent magnets	p	4	–
Rotor outer diameter	d_r	67	mm
Shaft diameter	d_{axis}	26	mm
Rotor core active length	L_{rot}	65	mm
Permanent magnets height	l_m	3.50	mm
Airgap length	l_g	0.50	mm
Pole arc/pole pitch ratio	$2a$	65	%

names are used): (a) *low carbon steel 1020*, (b) *silicon steel M-36*, (c) *cobalt steel 2V permendur*, (d) *nickel steel 4750 cross* and (e) *alloy powder core Koolmu 90*. *Low carbon steel 1020* is an alloy which contains 0.18% of carbon. It also contains manganese, silicon, phosphorus and sulphur at low levels. This steel is the most widely used material in electrical machines especially in cases where high core losses are acceptable and the low cost of the final product is a priority. Non-oriented silicon steels are the most commonly used materials for PMSMs. Their high permeability, low coercivity, low losses and ductile properties made them the most suitable steels for high speed and high efficiency motors with permanent magnets. *Silicon steel M-36* consists of 96% iron, 0.5% silicon, 1% aluminium and 0.5% manganese. *Cobalt steel 2V permendur* is a soft magnetic alloy which consists of 48% cobalt, 2% vanadium and 50% iron and has been primarily used as the magnetic core material in electrical machines due to its high permeability values at very high magnetic flux densities. The magnetic characteristics of this alloy permit the mass reduction of copper turns and insulation in

PMSMs when compared to other electrical steels. However, its price remains very high and it is preferred for low and medium voltage PMSMs. *Nickel steel 4750 cross* is a 47.5% nickel-iron alloy which combines a high saturation flux density permeability and low core losses. This material is known for its ability to operate under high mechanical stress and its good magnetic properties. Finally, *alloy powder Koolmu 90* is iron alloy in the form of powder, epoxy resin and glass or carbon fibre. It presents low core losses and ease of machining, low magnetic permeability, a relatively flat magnetization curve and a relatively low maximum permissible flux density. Reader can refer to [27] for more information about the materials that were used here for stator and rotor cores. Also, it must be mentioned that material with non-magnetic properties has been used for the construction of the motor's shaft.

2.2. Mathematical background

In this Section the mathematical background and the equations that govern the magnetic field analysis of PMSMs are thoroughly described. In order to evaluate the performance of a motor of this type, it is necessary to solve Maxwell's equations, which are given in Equations (2), where \vec{H} is the magnetic field vector, \vec{J} is the current density vector, \vec{E} is the electric field vector, \vec{B} is the magnetic flux density vector, \vec{D} is the electric displacement vector, ρ is the electric charge density and t is the time.

$$\begin{aligned} \text{a. } \vec{\nabla} \times \vec{H} &= \vec{J}, & \text{b. } \vec{\nabla} \times \vec{E} &= -\frac{\partial \vec{B}}{\partial t} \\ \text{c. } \vec{\nabla} \cdot \vec{D} &= \rho, & \text{d. } \vec{\nabla} \cdot \vec{B} &= 0. \end{aligned} \quad (2)$$

Generally, it is often more convenient when solving Maxwell's equations to express the fields in term of potentials and then deriving the fields from these. Also, it is required to introduce in these equations the magnetic vector potential \vec{A} . Taking the above into account Equations (3)–(4) can be derived. In (4), μ_0 is the magnetic permeability of vacuum. Combining the following equations with the expression given in (2a), the expression of (4) can be rewritten as stated in (5).

$$\vec{B} = \vec{\nabla} \times \vec{A} \Rightarrow \vec{\nabla} \cdot \vec{B} = \vec{\nabla} \cdot (\vec{\nabla} \times \vec{A}) = 0, \quad (3)$$

$$\vec{\nabla} \times (\vec{\nabla} \times \vec{A}) = \mu_0 \vec{J} \Rightarrow \vec{\nabla} \cdot (\vec{\nabla} \times \vec{A}) - \vec{\nabla}^2 \times \vec{A} = \mu_0 \vec{J}, \quad (4)$$

$$\vec{\nabla} \times \vec{H} = \vec{\nabla} \times \frac{\vec{B}}{\mu} = \vec{\nabla} \times \frac{1}{\mu} \vec{\nabla} \times \vec{A} = \vec{J}. \quad (5)$$

In the case of 2D magnetic field analysis and when the Cartesian coordinates are used, the current density vector \vec{J} has only a z-axis component. Consequently, the magnetic vector potential \vec{A} has also a z-axis component, i.e. \vec{A} is parallel to vector \vec{J} . Then these two vectors can be expressed as $\vec{J} = [0, 0, J_z]$ and $\vec{A} = [0, 0, A_z]$.

Thus, (5) can now be expressed as:

$$\frac{\partial}{\partial x} \frac{1}{\mu_x} \frac{\partial A_z}{\partial x} + \frac{\partial}{\partial y} \frac{1}{\mu_y} \frac{\partial A_z}{\partial y} = -J_z, \quad (6)$$

where μ_x and μ_y are the magnetic permeability of the material in x-axis and y-axis direction, respectively. If homogeneous materials are used for the construction of the electrical

machines and can be considered equal to the material's magnetic permeability μ and consequently (6) can be set as,

$$\frac{\partial^2 A_z}{\partial x^2} + \frac{\partial^2 A_z}{\partial y^2} = -\mu J_z. \quad (7)$$

Then the magnetic flux distribution can be obtained using (8), where B_x , B_y and B_z are the x , y and z -components of the magnetic flux density.

$$\vec{B} = \vec{\nabla} \times \vec{A} = \vec{\nabla} \times [0, 0, A_z] = \left[\frac{\partial A_z}{\partial y}, -\frac{\partial A_z}{\partial x}, 0 \right] \Rightarrow \begin{cases} B_x = \frac{\partial A_z}{\partial y} \\ B_y = -\frac{\partial A_z}{\partial x} \\ B_z = 0 \end{cases} \quad (8)$$

The above expression is referred in Cartesian coordinates. In the 2D model that was developed here for the magnetic field analysis of the PMSM used here, polar coordinates have been adopted and therefore it was necessary this expression to be transformed in them. For this purpose, the transformation formula described by (9)–(10) was implemented. In these Equations (x, y) are the Cartesian coordinates, (r, ϕ) are the polar ones, while $\vec{i}_x, \vec{i}_y, \vec{i}_r$ and \vec{i}_ϕ are the unit vectors of x, y, r and ϕ axis components, respectively.

$$\frac{x}{r} = \cos \varphi, \frac{y}{r} = \sin \varphi, r = \sqrt{x^2 + y^2}, \quad (9)$$

$$\begin{aligned} \vec{i}_r &= \cos \varphi \vec{i}_x + \sin \varphi \vec{i}_y, \\ \vec{i}_\phi &= -\sin \varphi \vec{i}_x + \cos \varphi \vec{i}_y. \end{aligned} \quad (10)$$

If the magnetic flux density is considered equal to $\vec{B} = B_x \vec{i}_x + B_y \vec{i}_y$, the radial component B_r and the tangential component B_ϕ of the magnetic flux density can be calculated as in (11)–(12). Finally, the amplitude of the total magnetic flux density B_{tot} is obtained by applying Equation (13):

$$\begin{aligned} B_r &= \vec{B} \cdot \vec{i}_r = (B_x \vec{i}_x + B_y \vec{i}_y) (\cos \varphi \vec{i}_x + \sin \varphi \vec{i}_y) \\ &= B_x \cos \varphi + B_y \sin \varphi \Rightarrow B_r = \frac{B_x x + B_y y}{r}, \end{aligned} \quad (11)$$

$$\begin{aligned} B_\phi &= \vec{B} \cdot \vec{i}_\phi = (B_x \vec{i}_x + B_y \vec{i}_y) (-\sin \varphi \vec{i}_x + \cos \varphi \vec{i}_y) \\ &= -B_x \sin \varphi + B_y \cos \varphi \Rightarrow B_\phi = \frac{-B_x y + B_y x}{r}, \end{aligned} \quad (12)$$

$$B_{tot} = \sqrt{B_r^2 + B_\phi^2}. \quad (13)$$

Furthermore, it must be mentioned that the same equations can be applied for the estimation of the magnetic flux density distribution in the case of 3D analysis, in which cylindrical coordinates have been adopted. The reason for this is that the investigated PMSM presents no variation in the z -axis and the implementation of the transformation from the Cartesian to cylindrical coordinates lead to the same expressions.

Moreover, among other electromechanical quantities, it is essential to determine motor's output power and the cogging torque. The latter one is an inherent characteristic of slotted PMSMs. It is caused by the interaction of the permanent magnets with the

stator teeth and can lead to torque ripple, vibration and noise during operation in electrical machines with permanent magnets. It is crucial for the designer to estimate the amplitude of cogging torque with accuracy through the magnetic field analysis in order to eliminate it by adjusting properly motor's geometrical parameters. Several techniques have been proposed so far for the calculation of the magnetic forces and torque using finite-element analysis. A commonly used methodology is based on the integration of Maxwell's stress tensor according to:

$$T_e = \oint_S \bar{r} \times \bar{\sigma} \cdot d\bar{S} = \oint_S \bar{r} \times \left[\frac{1}{\mu_0} (\bar{B} \cdot \hat{n}) \bar{B} - \frac{1}{2\mu_0} \bar{B}^2 \cdot \hat{n} \right] \cdot d\bar{S}, \quad (14)$$

where $\bar{\sigma}$ is the Maxwell's stress tensor, \hat{n} is the unit normal vector of the interaction surface, \bar{B} is the magnetic flux density vector in the middle of the airgap and \bar{r} is the unit vector of r -coordinate of the cylindrical coordinate system. A variation of the aforementioned approach was proposed in [28] for the case of 2D analysis, as the integration surface area can be reduced to a linear integral along the circumference of the airgap. If we consider then that the integration will be performed along the path that the circumference of a circle with radius r creates, the torque can be obtained from:

$$T_e = \frac{1}{\mu_0} \int_0^{2\pi} r^2 B_r B_\phi d\varphi. \quad (15)$$

The value of radius r varies between the radii r_s and r_r , which defines the two circles that have been created in order to be located outside and inside, respectively of the circles that pass through the middle of the airgap. Thus, (15) can be rewritten as in (16), where L is the axial length of the PMSM:

$$\begin{aligned} T_e (r_s - r_r) &= \int_{r_r}^{r_s} T_e dr = \frac{L}{\mu_0} \int_{r_r}^{r_s} \left[\int_0^{2\pi} r B_r B_\phi d\varphi \right] dr = \frac{L}{\mu_0} \int_S r B_r B_\phi dS \\ \Rightarrow T_e &= \frac{L}{\mu_0 (r_s - r_r)} \cdot \int_S r B_r B_\phi dS. \end{aligned} \quad (16)$$

This method has been used in this study for the calculation of the motor's output torque in the 2D analysis. For the case of the 3D model the original technique, based on the surface integration of Maxwell's stress tensor was implemented. The calculation of cogging torque was also based on the two aforementioned techniques. It must be mentioned here that the determination of this quantity requires the motor to be studied under no-load operation, i.e. when the three-phase winding is not excited and the magnetic field is only produced by the permanent magnets.

3. 2D analysis and results

The conduction of 2D magnetic field analysis of the adopted PMSM involves the problem definition, the solution estimation and the post-processing analysis of the derived results. The problem definition consists of (a) the development of the detailed motor's geometry based on the aforementioned design parameters, (b) the initialization of a large amount of variables in order to be utilized in the simulation or shown as results, (c) the selection of materials for the different parts of the model and (d) the specification of the appropriate physical relations that describe the problem. Next, the mesh quality and the simulation

properties had to be determined. Then a mesh was built which divided the geometry into elements and nodes, the simulation was performed and the solution was estimated. Finally, various electromagnetic quantities, such as the flux density distribution, output torque and cogging torque could be graphically represented. Similar process was also followed for the simulation in 3D. All simulations were performed by using the same computing system equipped with an Intel Core i-7-3520m processor at 2.90 GHz and 16 GB of RAM. Regarding the mesh quality, it was revealed after the conduction of plenty investigations that the elements density has a great impact on the solution accuracy. The accurate calculation of quantities, such as the torque, requires high mesh quality especially in the area of the air-gap. Taking into account the given computational resources and the above observation, an extremely fine mesh quality was selected for the area of permanent magnets, airgap and stator slots. An extra fine quality was preferred for the area of stator and rotor core, while a fine one was selected for motor's shaft. The above specifications led to the division of the model into 192,000 finite elements and the mesh in the area of airgap had the view that is shown in Figure 3.

At first, the total airgap magnetic flux density versus the length of the airgap circumference was estimated. This quantity is depicted in Figure 4 for each one of the used ferromagnetic materials. The total magnetic flux density is produced by the interaction between the magnetic field derived by the stator windings currents and the constant magnetic field generated by the rotor permanent magnets. All the displayed waveforms were acquired at the same moment during the time-dependent analysis in order the results to be comparable to each other. At the selected moment the rotor has been rotated by 288 degrees with respect to its initial position. A significant variation is observed for the value of the total magnetic flux density at specific parts of the curves. The decrease of its value

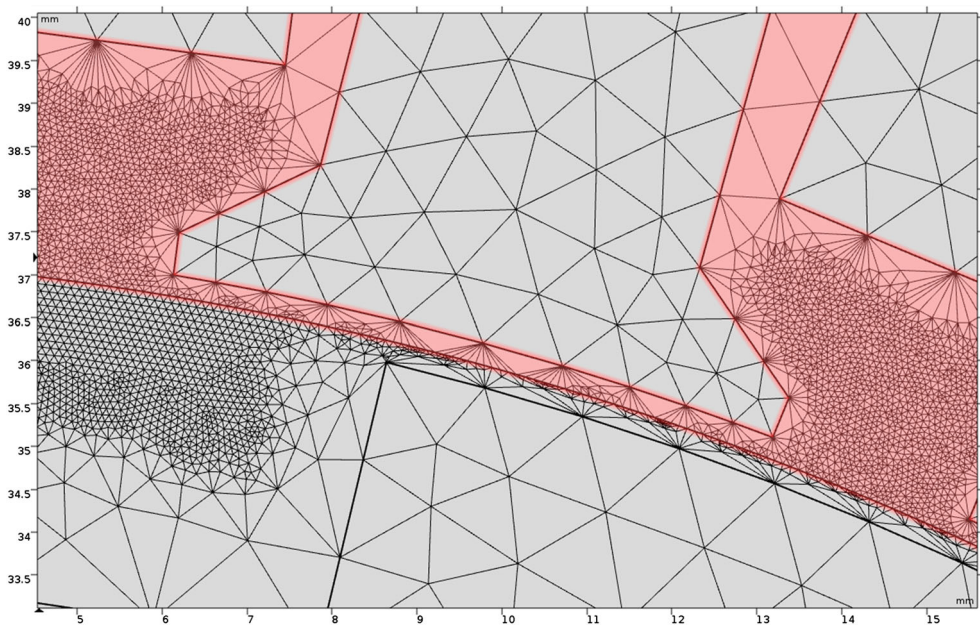


Figure 3. A detailed view of the mesh quality in the area of airgap, permanent magnets and stator teeth.

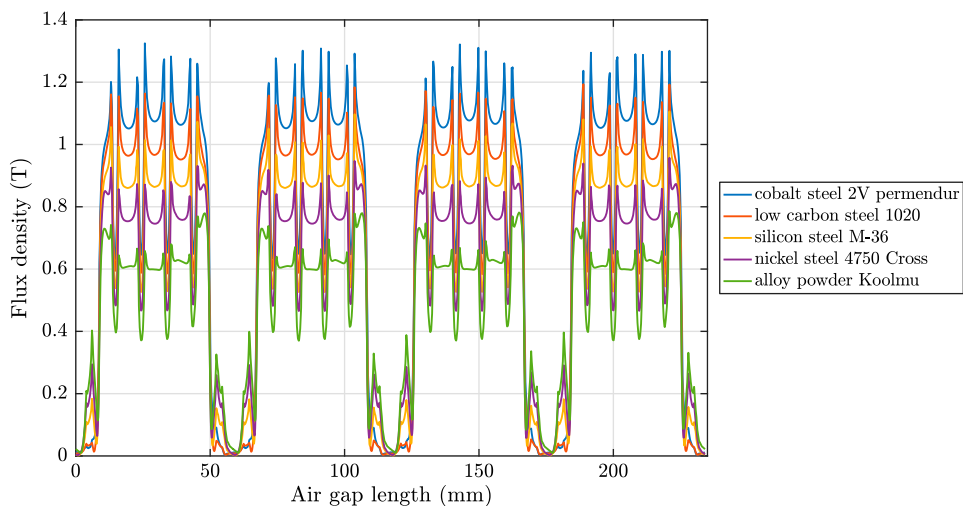


Figure 4. Total air gap flux density distribution in 2D obtained for each one of the five used materials.

is due to the slot opening effect. When the permanent magnets face the slot opening the magnitude of flux density is reduced as a significant number of flux lines leaks in the air. This reduction occurs for a length equal to the geometrical parameter b_{s0} (according to Figure 2).

The intensity of this phenomenon depends on the slot opening width and the interaction between the permanent magnets and the ferromagnetic material that is used for the construction of the stator teeth.

The different flux density distribution for each material, taking also into account the slot opening effect, is easily observed based on the curves that are presented in Figure 4. Consequently, the *rms* value of the flux density is different for each material. For instance, when the *silicon steel M-36* is used, the *rms* value of the total flux density is equal to 0.776 T. The maximum value has been achieved in the case of *cobalt steel 2V permendur*, while the minimum one has been noticed in the case of *alloy powder Koolmu*, as their values are equal to 0.933 and 0.558 T, respectively. The *rms* values of this quantity are given for each material in Table 4. At the same Table, the percentage variation of the *rms* value derived from each case study taking as reference the value obtained for the *silicon steel M-36* is also provided. It is considered that the accurate estimation of the shape, the maximum amplitude and the *rms* value of this specific quantity is very essential for the engineers. Indeed, if the shape of the flux density distribution is not the desirable, phenomena such as torque ripple,

Table 4. Comparison of the airgap total flux density *rms* value achieved for various materials using the 2D model.

Material	Airgap B_{tot} RMS value (T)	Variation (%)
silicon steel M-36	0.766	0.000
nickel steel 4750 cross	0.680	−11.227
cobalt steel 2V permendur	0.933	+21.802
low carbon steel 1020	0.847	+10.574
alloy powder core Koolmu 90	0.558	−37.276

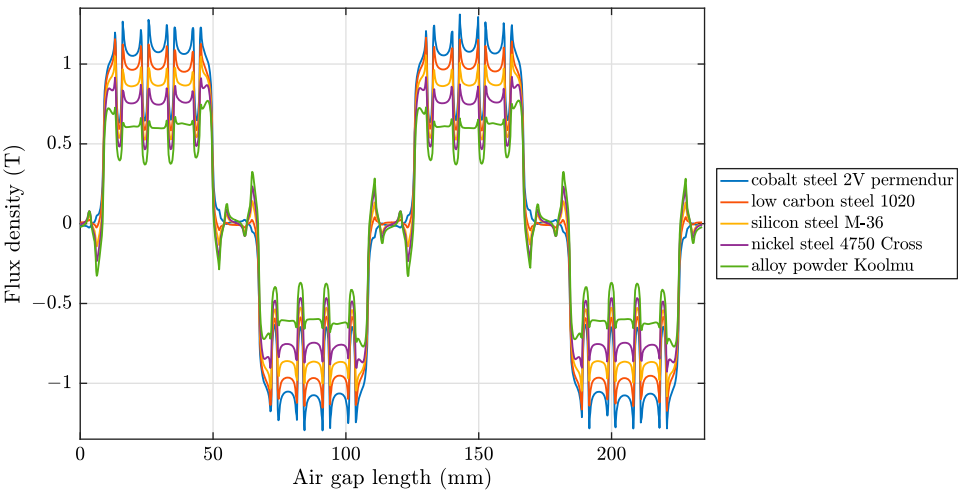


Figure 5. Radial component of the airgap flux density distribution in 2D for each one of the five used materials.

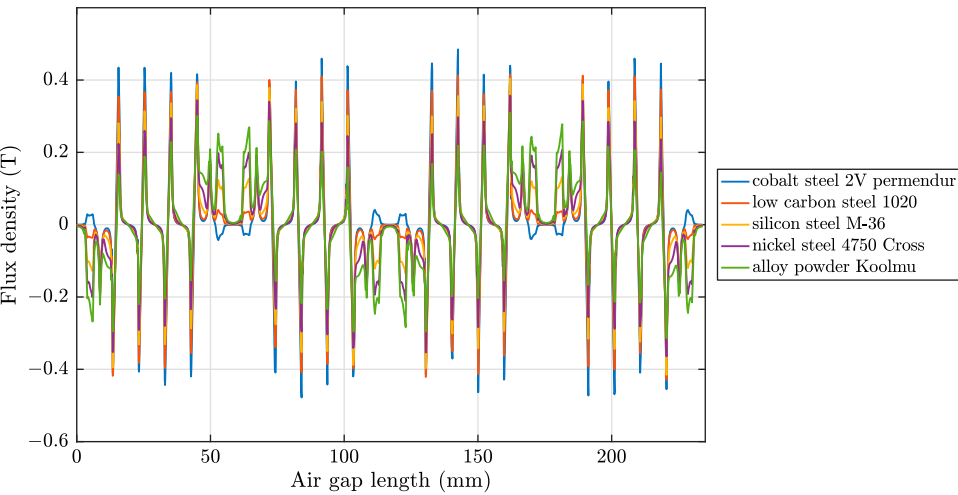


Figure 6. Tangential component of the airgap flux density distribution in 2D for each one of the five used materials.

vibration or even noise during the motor’s operation can be occurred. The determination of the maximum amplitude and the flux density *rms* value is important in order to ensure that the motor’s nominal requirements are fulfilled. Otherwise, the motor’s design specifications have to be reconsidered.

Apart from the total flux density distribution, its radial and tangential components are also of great interest. The waveforms of the aforementioned components are illustrated in Figures 5 and 6 respectively. As it can be seen, the radial component presents higher amplitude than the tangential one and consequently determines to a greater extent the amplitude and the shape of the total flux density distribution. Similar conclusions can be made as the ones derived from the analysis of the total flux density distribution. Important

differences are also observed with respect to the amplitude of the waveforms obtained for each material.

On the other hand, the shape of the five curves is quite the same. The value of the tangential component presents higher variation along with the length of the circumference of the airgap. Moreover, the determination of the components of the airgap flux density is crucial for the calculation of the motor's output torque based on the method which was described in the Section 2.2. The torque versus time in the case of *silicon steel M-36* is given in Figure 7. From this figure it can be observed that the motor's synchronization is achieved after approximately 0.04 sec. The average output torque is equal to 3.506 Nm, while the maximum torque during motor's starting performance is equal to 5.105 Nm. Also, the torque ripple is equal to 7.65%. This quantity is evaluated by calculating the ratio of the difference between the maximum and the minimum recorded torque value to the mean output torque after the synchronization. The incorporation of various ferromagnetic materials incorporated in the 2D model affects significantly the motor's output torque as the two components of the airgap flux density are varied according to material's characteristics. The mean output torque achieved for each material as well as the percentage variation taking as reference the mean value of the torque in the case of *silicon steel M-36* are given in Table 5.

Based on the obtained results presented in Tables 4 and 5 it can be concluded that motor's torque varies in a way similar to the total airgap flux density variation. For example,

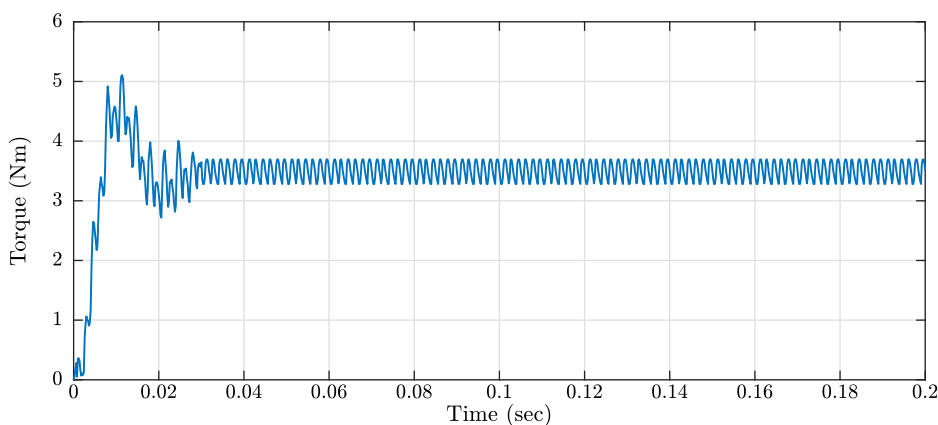


Figure 7. The motor's output torque versus time obtained through 2D analysis when *silicon steel M-36* was used for both the stator and rotor cores.

Table 5. The motor's average output torque obtained through 2D analysis for each one of the five used materials.

Material	Mean of PMSM output torque (Nm)	Variation (%)
silicon steel M-36	3.506	0.000
nickel steel 4750 cross	3.113	−11.209
cobalt steel 2V Permendur	4.275	+21.934
low carbon steel 1020	3.881	+10.696
alloy powder core Koolmu 90	2.556	−37.167

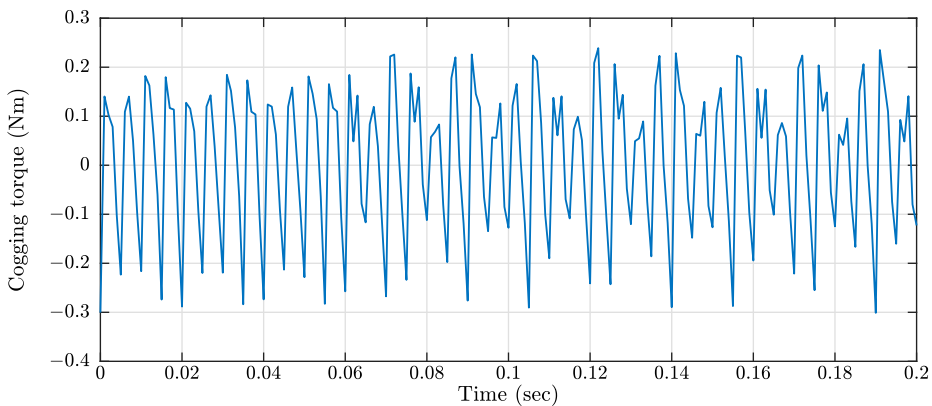


Figure 8. The cogging torque obtained through 2D analysis when *silicon steel M-36* was used for both the stator and rotor cores.

if the two components of airgap flux density are increased, a corresponding increment is noticed for the motor's output torque too. Additionally, Figure 8 depicts the cogging torque versus time when the *silicon steel M-36* was used for stator and rotor cores. The maximum amplitude of the cogging torque is equal to 0.18 Nm. This value can be judged acceptable compared to the motor's nominal output torque (i.e. 5.14%) and is related with the specific design considerations of the adopted PMSM. This value could be lower either if a different stator slots/poles combination was selected or the slot opening width was shorter. A careful determination of permanent magnets dimensions and especially the pole arc to pole pitch ratio (i.e. $2a$ with respect to Figure 2) could also eliminate the amplitude of the cogging torque. However, this procedure was not one of the main scopes of this study.

Finally, the distribution of the magnetic flux density throughout the motor's overall structure and for each one the used materials is depicted in Figure 9. Although the stator windings of the motor are excited with the same amount of current for each one of the examined cases, a significant difference in the magnetic flux density distribution is observed. In order for the results to be comparable to each other, the same maximum and minimum value has been set during the illustration of the flux density distribution (coloured legend). Specifically, when the *alloy powder Koolmu* is used (Figure 9(a)) there is a little magnetic induction and the capabilities of the material are not fully exploited, since the maximum recorded value does not exceed 1.2 T. In the case of *cobalt steel 2V permendur* (Figure 9(b)) the observed values are higher than 1.8 T for the most part of the motor. This high value is due to the material's high magnetic permeability resulting in high flux values in the stator and rotor cores and also in low flux leakage in the air. Thus, in some narrow motor's parts, a high flux density value is reached. The comparison of this value with the magnetization curve of the specific material revealed that the motor can operate without being drawn into core saturation as its saturation value is around 2 T. On the other hand, flux density values higher than 1.5 T are obtained in the case of *low carbon steel 1020* (Figure 9(c)) and consequently this leads to the saturation of the material in the area of stator core and teeth. When *nickel steel 4750 cross* is used (Figure 9(d)) the maximum value does not exceed 1.5 T for most parts of the motor. The motor's shaft is the only exception, since slightly higher values are observed in this area. When *silicon steel M-36* is used (Figure 9(e))

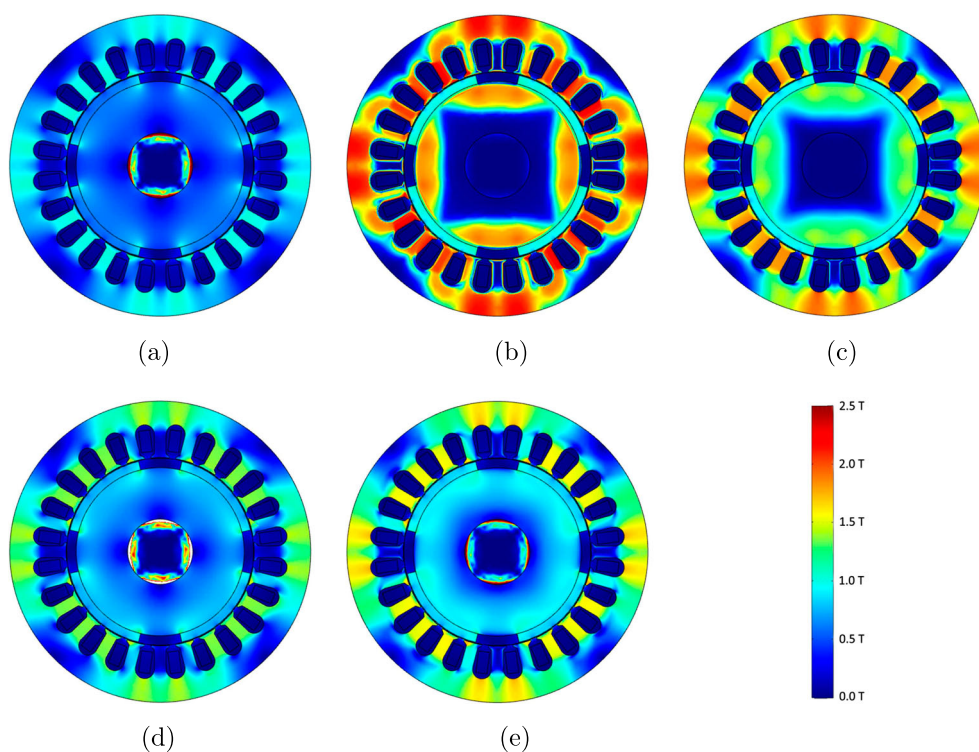


Figure 9. Flux density distribution on the overall 2D PMSM's model corresponding to each one of the five used materials for the construction of the rotor and stator core: (a) *alloy powder Koolmu 90*, (b) *cobalt steel 2V permendur*, (c) *low carbon steel 1020*, (d) *nickel steel 4750 cross* and (e) *silicon steel M-36*.

the machine core operates at flux density values from 0.8 to 1.6 T. The maximum recorded value is far enough from the saturation point based on the magnetization curve of the material. At the area of the rotor core, the airgap and the permanent magnets the flux density is equal to 1.4, 0.8 and 1.3 T, respectively.

4. 3D analysis and results

In this Section, the derived results through 3D magnetic field analysis are presented and discussed. The basic steps that were followed for the conduction of the 2D analysis are also adopted in the case of the 3D one, while at the same time similar investigations were carried out aiming the results to be analytically compared to each other in the next Section. However, significant modifications were made in order the specific problem requirements to be fulfilled. When a 3D analysis is preferred the mesh generation and the simulation performance is a time-consuming and demanding process. Furthermore, increased computational resources are required. The mesh can be composed of tetrahedral, hexahedral, prisms or pyramids elements. The conduction of a series of investigations revealed that the utilization of hexahedral or prisms elements leads to the reduction of the total number of the elements that is required for the mesh generation. This reduction limits the

computational resources that are necessary for the implementation of the simulation. Thus, in our case study the hexahedral elements had been used.

At first, the total airgap magnetic flux density and its components (i.e. its radial and tangential component) were evaluated. These quantities are depicted versus the length of the airgap circumference in Figures 10–12 for each one of the used ferromagnetic materials. All the displayed waveforms were acquired at the same moment during the time-dependent analysis in order the results to be comparable to each other. At the selected time instant, the rotor has been rotated by 288 degrees with respect to its initial position. As it can be seen from these figures, the tangential component of the magnetic flux density presents

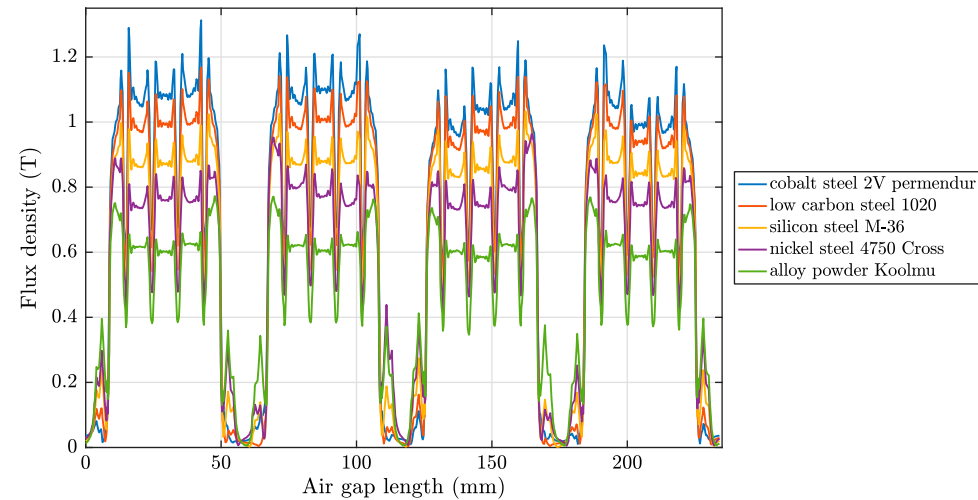


Figure 10. Total air gap flux density distribution in 3D obtained for each one of the 5 used materials.

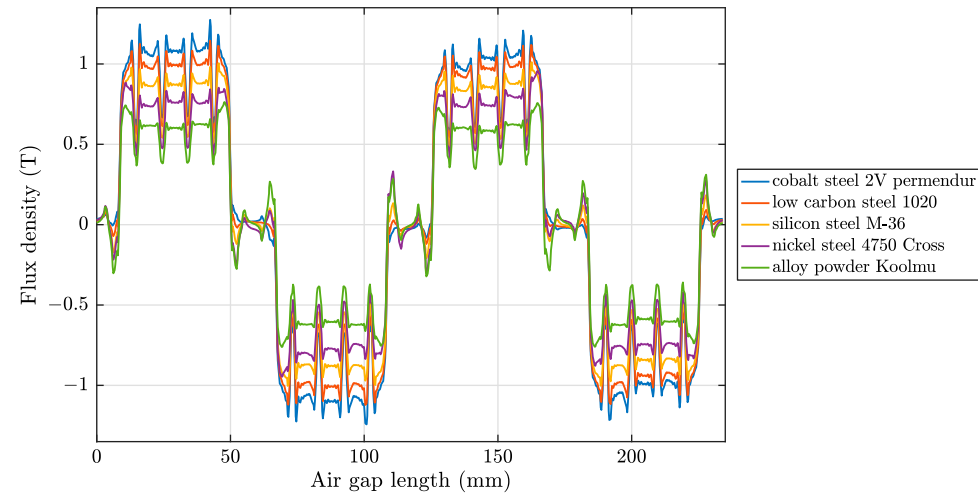


Figure 11. Radial component of the airgap flux density distribution in 3D for each one of the five used materials.

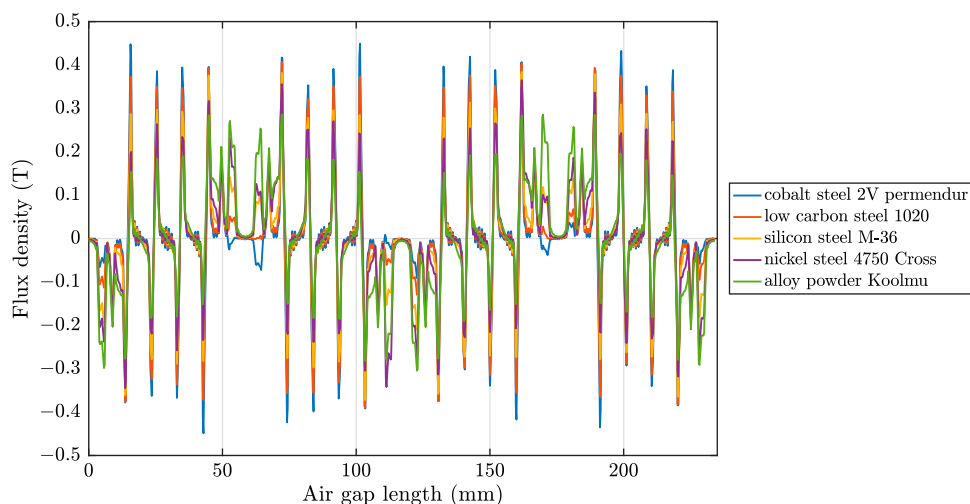


Figure 12. Tangential component of the airgap flux density distribution in 3D for each one of the five used materials.

Table 6. Comparison of the airgap total flux density *rms* value achieved for various materials and by using the 3D model.

Material	Airgap B_{tot} RMS value (T)	Variation (%)
silicon steel M-36	0.705	0.000
nickel steel 4750 cross	0.632	−10.364
cobalt steel 2V Permendur	0.842	+19.451
low carbon steel 1020	0.787	+11.675
alloy powder core Koolmu 90	0.520	−26.260

lower amplitude than the radial one and higher variation along with the length of the airgap circumference. The impact of the radial component on the configuration of the total flux density is evident. Significant differences in the curves are also observed for the various examined materials. The *rms* value of the derived total flux density is equal to 0.705 T when *silicon steel M-36* is used. In the case of *nickel steel 4750 cross* a lower value by 10.36% has been achieved compared to the one obtained for the *silicon steel M-36*. The maximum *rms* value is observed for the *cobalt steel 2V permendur* and the minimum one for the *alloy powder Koolmu*, as their values are equal to 0.84 T and 0.52 T, respectively. The *rms* values of the total flux density obtained for each material and the percentage variation taking as reference the value derived when *silicon steel M-36* was used are provided in Table 6.

After the calculation of the airgap flux density components, the estimation of the motor's output torque and the cogging torque had been followed based on the method described in Section 2.2. These two quantities are given in Figures 13 and 14. From the first figure, it can be observed that the motor's average output torque is equal to 3.33 Nm when *silicon steel M-36* is used for the construction of the stator and rotor core. The average torque value is lower by 5.04% than the corresponding one derived through the 2D magnetic field analysis. The torque ripple has been calculated equal to 10.75% Nm and maximum torque during motor's starting performance is 4.84 Nm. The torque ripple value has been found increased compared to the value that was obtained from the 2D analysis. The average output torque

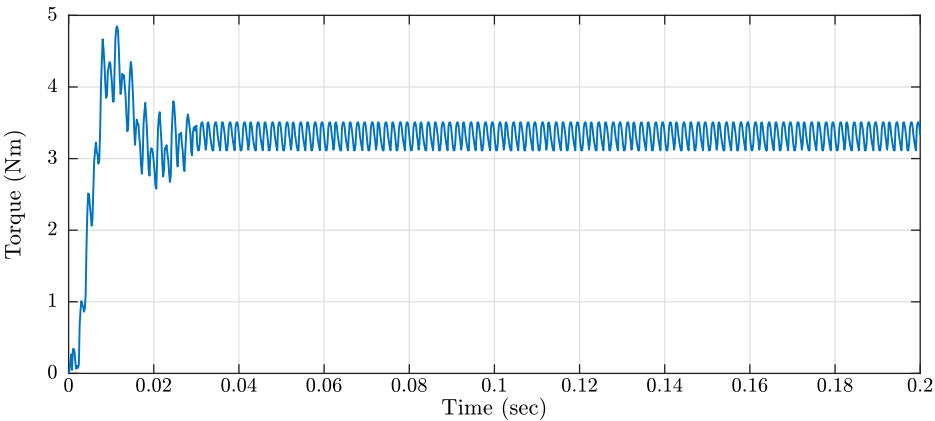


Figure 13. The motor’s output torque versus time obtained through 3D analysis when *silicon steel M-36* was used for both the stator and rotor cores.

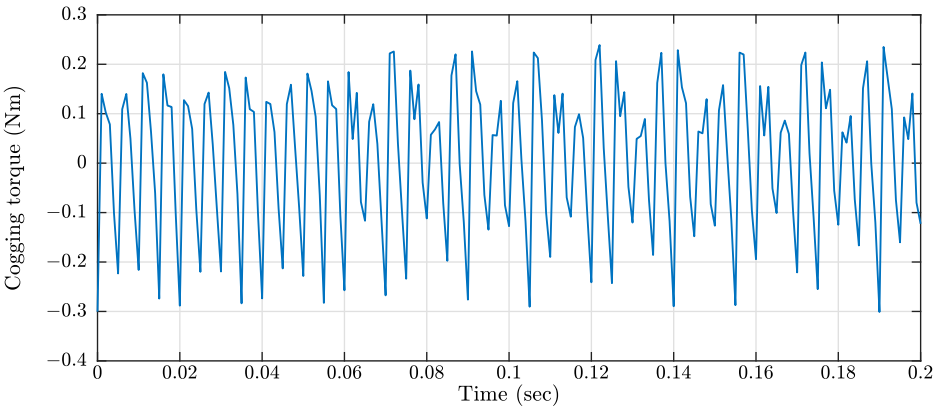


Figure 14. The cogging torque obtained through 3D analysis when *silicon steel M-36* was used for both the stator and rotor cores.

Table 7. The motor’s average output torque obtained through 3D analysis for each one of the five used materials.

Material	Mean of PMSM output torque (Nm)	Variation (%)
silicon steel M-36	3.329	0.000
nickel steel 4750 cross	2.992	−10.116
cobalt steel 2V Permendur	3.970	+19.257
low carbon steel 1020	3.690	+10.845
alloy powder core Koolmu 90	2.392	−28.145

achieved for each material as well as the percentage variation taking as reference the mean value of the torque derived in the case of *silicon steel M-36* are presented in Table 7. Similar conclusions to those drawn by the data provided in Table 5 can also be reached here. Regarding the cogging torque, its maximum amplitude is slightly decreased compared to the corresponding amplitude calculated through the 2D analysis.

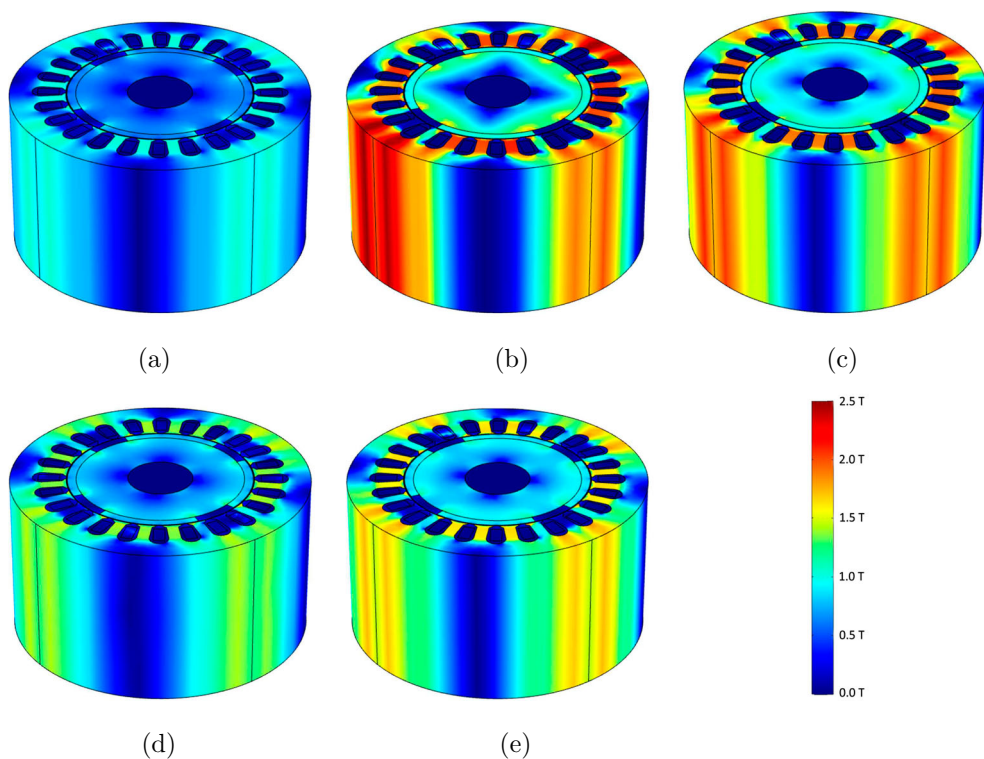


Figure 15. Flux density distribution on the overall 3D PMSM's model corresponding to each one of the five used materials for the construction of the rotor and stator core: (a) *alloy powder Koolmu 90*, (b) *cobalt steel 2V permendur*, (c) *low carbon steel 1020*, (d) *nickel steel 4750 cross* and (e) *silicon steel M-36*.

It is clear so far that the difference between the 2D and the 3D analysis results is remarkable. Further investigation on the accuracy of the results is going to be conducted in the next Section. Furthermore, the flux density distribution on the 3D model of the adopted PMSM is depicted for each one of the used materials in Figure 15. From this figure, the following can be seen: (a) the motor core has great possibility to be drawn into saturation in the stator yoke and teeth, (b) a deep saturation has been detected when the material *low carbon steel 1020* is used, (c) low magnetic induction occurs in the case of *nickel steel 4750 cross*, since the maximum recorded value is not higher than 0.52 T and (d) the high values of flux density when *cobalt steel 2V permendur* is used have not led to his saturation, as these values are far away from the saturation point based on material's magnetization curve.

5. Overall discussion

5.1. Comparison of the results

The performance of 2D and 3D magnetic field analysis and their corresponding results are compared and discussed here. Their comparison is based on the results accuracy, the percentage error between the derived values, the computational time and the required computing storage space. For this purpose, the airgap total flux density is demonstrated in Figure 16 for both 2D and 3D analysis, when *silicon steel M-36* is applied for stator and rotor

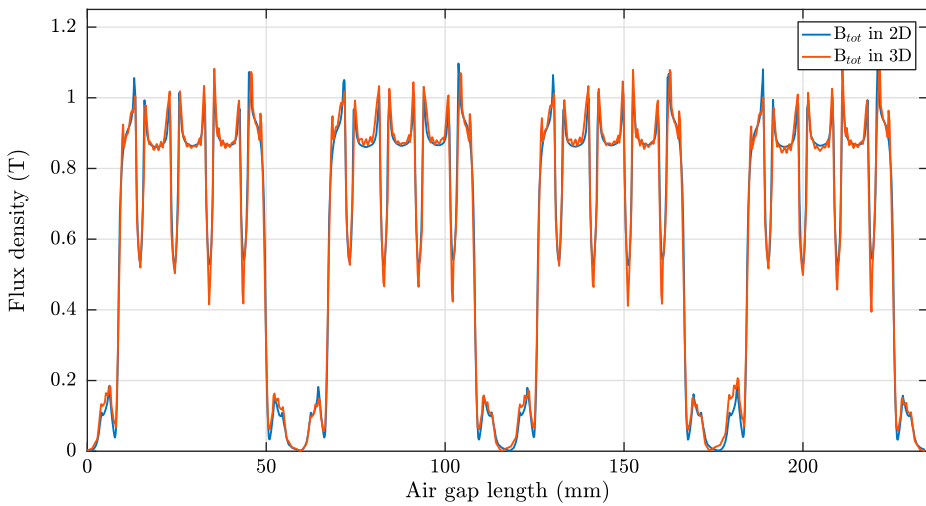


Figure 16. Comparison of the airgap total flux density distribution obtained from the 2D and 3D analysis.

cores. A first glance on this figure reveals that there is no significant difference between the derived results. However, the *rms* value of the total flux density distribution for 2D and 3D analysis was calculated equal to 0.766 and 0.705 T, respectively. Thus, there is a reduction of 7.96% for this value when the results are obtained through the 3D magnetic field analysis. So, a further investigation was performed to clarify this issue. Firstly, in order to determine the variation of the two waveforms, it was decided to calculate the area under the one-quarter of the two curves (i.e. corresponding to one magnetic pole of the motor). The one-quarter of the two curves is illustrated in Figure 17. Next, these one-quarter curves were divided into three sub-regions (let us call them sub-regions A, B and C) in such a way

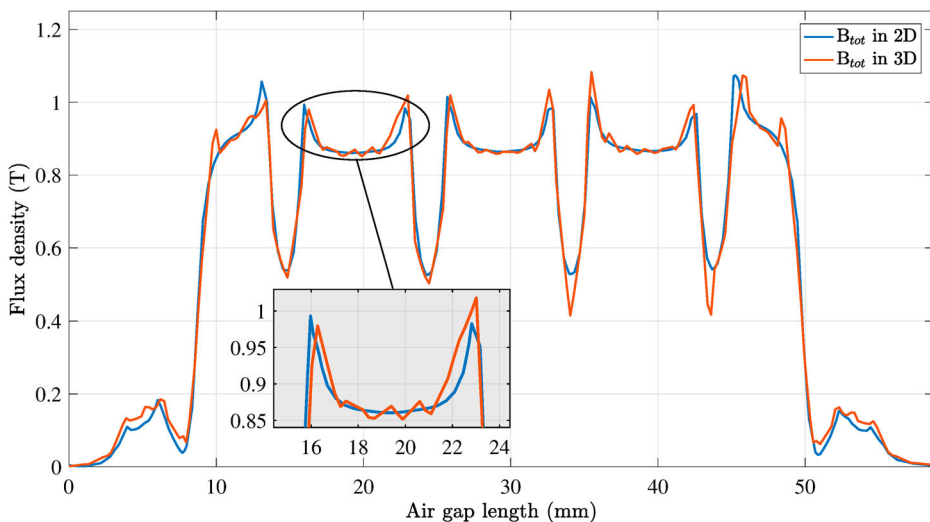


Figure 17. Comparison of the one-quarter curve of the airgap total flux density distribution obtained through 2D and 3D analysis.

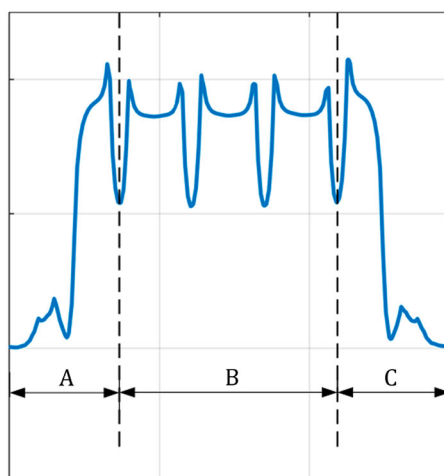


Figure 18. The one-quarter curve divided into three sub-regions.

Table 8. Comparison of the area enclosed under the total curve and the three sub-regions obtained through 2D and 3D analysis.

	Total Area	Area of Region A	Area of Region B	Area of Region C	% variation of Total Area	% variation of region A	% variation of region B	% variation of region C
2D	35.603	5.617	24.294	5.692	+1.413	+9.827	−0.757	+2.372
3D	36.106	6.169	24.110	5.827				

as it is depicted in Figure 18. The area of the total region and of each one of three sub-regions as well as the percentage variation taking as reference the results derived from the 2D analysis are given analytically in Table 8. From these results, the followings are found:

- the one-quarter curve obtained through the 3D analysis encloses larger area compared to the corresponding one obtained through the 2D analysis,
- the percentage variation among the aforementioned areas is equal to 1.415%,
- among the other sub-regions areas the highest variation is observed in the sub-region A and the minimum one in sub-region B,
- the relatively high percentage variation observed in the sub-region A could explain the difference between the aforementioned calculated rms values of B_{tot} and,
- the percentage variation between the areas under the two curves at the sub-region B seems to be quite low despite the impact of the slot opening effect.

The rms values of B_{tot} for each one of the used material and for both the 2D and 3D analysis are also presented in Table 9. The difference between the corresponding values varies approximately from 7% to 9.75%. The lowest values were always recorded for the 3D analysis. Moreover, the curve of Figure 17 presents some fluctuation at sub-region B where a few “spikes” are observed. These spikes seem to be estimated only through the 3D analysis. If this fluctuation is low, there is no problem if these spikes are not to be perceived through the simulation. However, when the fluctuation is intense, it is crucial for the engineers to know its existence, especially when the shape of the total airgap flux density is of great

Table 9. The *rms* value of the airgap total flux density distribution as obtained through 2D and 3D analysis.

Material	RMS value of B_{tot} in airgap obtained through 2D (T)	RMS value of B_{tot} in airgap obtained through 3D (T)	Error (%)
Silicon steel M-36	0.766	0.705	−7.963
Nickel steel 4750 cross	0.680	0.632	−7.059
Cobalt steel 2V permendur	0.933	0.842	−9.753
Low carbon steel 1020	0.847	0.787	−7.084
Alloy powder Koolmu 90	0.558	0.520	−6.810

importance. Thus, considering this aspect, it seems that the 3D magnetic field analysis has a clear advantage over the 2D one, since it permits the more accurate evaluation of the airgap flux density, which is a quantity that has a great impact on motor’s behaviour.

The above consideration can also be confirmed if the radial and the tangential component of the airgap flux density are further analysed. By observing Figure 19, in which the radial component of the flux density is depicted, the two curves seem quite similar. On the other hand, when the one-quarter of the radial component curve is investigated the existence of some fluctuation is revealed, while at the same time the slot opening effect is more intense (Figure 20). No significant difference between the two types of analysis is observed when the tangential component of the flux density distribution (Figure 21) is examined.

Regarding the accuracy of the motor’s average output torque calculation, it was found that the percentage error of the 2D analysis varies from 3.8% to 7%. These values are considered to be high, but this can be explained by the fact that the torque was evaluated by using Arkkio’s method [28]. This methodology, as already mentioned, is based on the estimation of the radial and tangential component of the airgap flux density distribution for the calculation of the torque. Thus, if there is an error in the calculation of the two aforementioned quantities, an error will also be occurred in the output torque and cogging torque

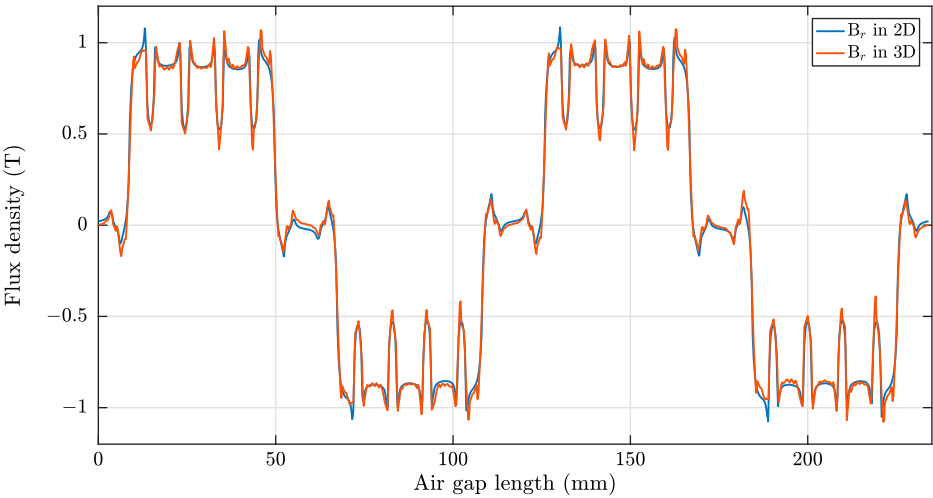


Figure 19. Comparison of the radial component of the airgap flux density distribution obtained through the 2D and 3D analysis.

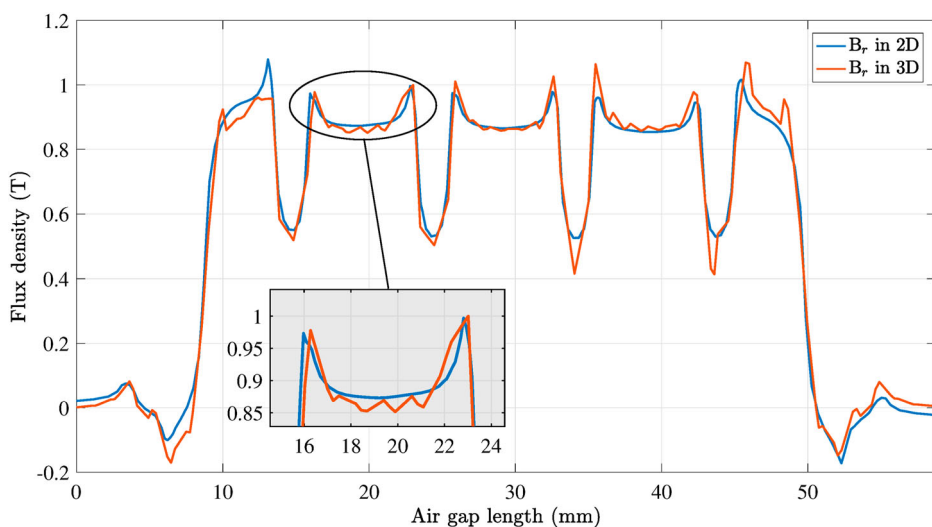


Figure 20. Comparison of the one-quarter curve of the radial component of the airgap flux density distribution obtained through 2D and 3D analysis.

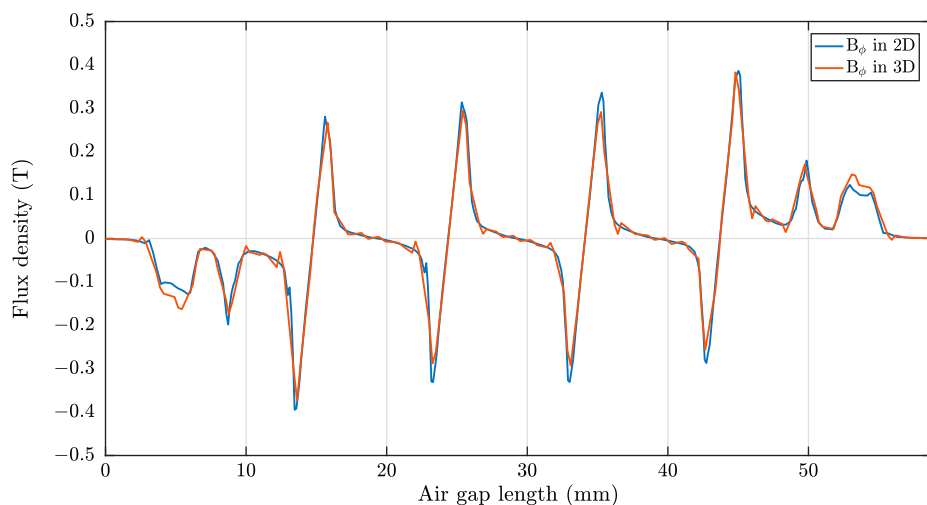


Figure 21. Comparison of the one-quarter curve of the tangential component of the airgap flux density distribution obtained through 2D and 3D analysis.

estimation. The amplitude of the cogging torque derived from the 3D analysis was lower by 4.65% than the corresponding one calculated by 2D analysis. The average motor's output torque obtained for each one of the used materials, as well as the percentage error of the 2D analysis torque results are given in Table 10.

Based on the above, it can be concluded that the 3D analysis produces more accurate results than the results obtained through the 2D analysis. However, the difference between the results and the percentage error seem to be significant only for a few electromagnetic quantities. For instance, the 3D analysis performance can lead to a more analytical and

Table 10. The adopted PMSM's average output torque obtained for each one of the used materials through the 2D and the 3D analysis.

Material	PMSM's average torque in 2D analysis (Nm)	PMSM's average torque in 3D analysis (Nm)	Error (%)
Silicon steel M-36	3.506	3.329	−5.048
Nickel steel 4750 cross	3.113	2.992	−3.887
Cobalt steel 2V permendur	4.275	3.970	−7.135
Low carbon steel 1020	3.881	3.620	−6.725
Alloy powder Koolmu 90	2.556	2.392	−6.416

accurate estimation of the torque and the airgap total flux density. Also, the impact of phenomena such as the slot opening effect is more distinct, while the existence of ripple or even spikes can be detected only in curves that have been acquired only through the 3D analysis.

On the other hand, the 2D analysis seems to be suitable enough for performance evaluation of the PMSM. The saturation of motor's core in different parts, such as the stator yoke or the stator teeth, can easily be detected as the relative derived results in our case study presented increased accuracy. This is of great importance for the overall PMSM design and performance analysis procedure, as the engineer has the opportunity to adjust the design parameters in order to achieve the desirable motor's behaviour. Apart from the accuracy issue, another aspect that must be discussed is the computational cost (i.e. time and resources) that is related with each type of magnetic field analysis. The simulation time for each type of analysis and for each one of the used materials is provided in Table 11. The 3D analysis requires significantly much longer time, as the simulation times were found 54 up to even 80 times higher than the corresponding ones of the 2D simulation. Moreover, the size of the files used in 3D analysis was 10 times greater than the size of files used in the 2D analysis. In the first case, the majority of the files presented a size equal to 16 GB, while in the 2D analysis the size of the most files was equal to only 1.5 GB.

5.2. Effect of induced electromotive force on PMSM's developed torque

The PMSM's developed torque has three components: (a) the reluctance torque, which comes as a result of the inductance value variation, (b) the cogging torque due to the interaction among the permanent magnets and the openings of the stator slots and (c) the mutual torque, which is produced by the interaction between the induced electromotive force (or back-emf) and the stator current. Among these torque's components the mutual

Table 11. Comparison of the simulation time required for the conduction of the 2D and 3D analysis.

Material	Simulation time in 2D analysis (hours)	Simulation time in 3D analysis (hours)
silicon steel M-36	0.22	17.00
nickel steel 4750 cross	0.27	19.67
cobalt steel 2Vpermendur	0.64	45.67
low carbon steel 1020	0.40	26.33
alloy powder core Koolmu 90	0.12	6.84

torque is the major one and thus the back-emf is directly related to the PMSM's performance, reliability and robustness [29]. During the motor's operation, any distortion of the back-emf will have great effect on the quality of the produced electromagnetic torque, as it influences its average value and can even deteriorate the torque's ripple. When the amount of ripple becomes high, extensive vibrations and noise occur. Therefore, the back-emf should be as close as to possible to a sine wave and have low harmonic content. Aiming to suppress the torque's ripple various machine and control techniques have been developed. When the control strategies are adopted, the on-load back-emf can improve the performance of the PMSM and guarantee low torque ripple and high efficiency. The back-emf is strongly dependent on several design parameters, such as the slots/poles combination, pole embrace, stator slot opening, permanent magnets' thickness, airgap length, number of coils and turns per coils, etc. These characteristics must be carefully selected during the PMSM's design procedure.

Additionally, the back-emf is heavily affected by plenty of electromagnetic quantities, such as the electric loading condition, the magnetic saturation level on the stator teeth surface, the flux-linkage waveform and the airgap flux density distribution. The airgap magnetic fields harmonics are reflected by the back-emf. In the case of serious distortion of the airgap flux density distribution the back-emf is also affected and finally, high torque pulsation (i.e. cogging torque and torque ripple) is provoked. For this reason, it is very important for the machine designer to detect spikes or dips on the total airgap flux density distribution during the early design stages. The analysis of both radial and tangential component of the airgap flux density can certainly contribute to this direction. As it was already proven by the results presented in this study, the 3D finite-element analysis leads to a more accurate assessment of the airgap flux density components and consequently the harmonic content of the airgap flux density and back-emf can be precisely determined.

6. Conclusions

The design procedure of PMSMs is quite demanding as it contains plenty of design variables which have to be specified, while at the same time a large amount of constraints have to be fulfilled. In electrical machines design area, the above process is based mostly on magnetic field analysis using FEM in order to evaluate the machine's performance. Also, it has to be performed a lot of times during the overall procedure either by using 2D or 3D models. Regarding the magnetic field analysis of PMSMs, there was no concrete proof of the level of the error arising from the use of 2D models and also it was not clear when this lack of accuracy could be considered as acceptable. In order to provide a reliable answer to this conflict a 2D and 3D model of the adopted PMSM was constructed in this study. After that, the conduction of several 2D and 3D simulations were performed and plenty of investigations were followed. Various ferromagnetic materials were used for the construction of the stator and rotor core, while at the same time a large amount of essential electromagnetic and electromechanical quantities, such as the flux density distribution, the cogging torque and motor's output power, etc. were calculated. The derived results were post-processed and compared to each other in order to specify the arising error and highlight its importance and its impact on the calculation of other quantities. For this purpose, the *rms* value of these quantities and the area under the obtained quantities curves were determined and compared. Moreover, the time burden and the required computational resources were

examined. The aforementioned process concluded several useful observations and recommendations. Among others it was concluded that the 3D analysis exhibits higher accuracy than the 2D one in the calculation of the total flux density (including its components) and motor's output torque. Also, the 3D analysis permits the observation of fluctuation on specific parts of the flux density waveform and the slot opening has a great effect on the shape of the curve. On the other hand, it was found that the percentage error of 2D analysis is relatively low for the calculation of the cogging torque and the detection of the stator and rotor core saturation. Thus, in such a case the engineer can use 2D analysis safely for an acceptable performance evaluation and there is no need to undergo extra computational cost arising from the utilization of the 3D analysis.

Disclosure statement

No potential conflict of interest was reported by the authors.

Notes on contributors

Maria C. Pechlivanidou received the Diploma Degree from the Dept. of Electrical and Computer Engineering (DECE), Democritus University of Thrace (DUTH), Xanthi, Greece, in 2017. She is currently pursuing her PhD degree in the School of Electrical and Computer Engineering, National Technical University of Athens (NTUA), Greece. Her research interests include analysis, design and optimization of permanent magnet machines for traction applications.

Ioannis D. Chasiotis received the Diploma Degree from the Dept. of Electrical and Computer Engineering (DECE), Democritus University of Thrace (DUTH), Xanthi, Hellas, in 2015. He is with the Electrical Machines Laboratory of the same Department where he is currently pursuing his PhD degree. His research interests are in the area of electrical machines design, the incorporation of artificial intelligence methods in the design process and the development of permanent magnet synchronous and induction machines with characteristics of high power density and high efficiency.

Yannis L. Karnavas received the Diploma Degree and his PhD from the Dept. of Electrical and Computer Engineering (DECE), Democritus University of Thrace (DUTH), Xanthi, Hellas, in 1994 and 2002 respectively. From 2004 to 2013 was Director of the Electrical Machines & Electrical Installations Laboratories of Dept. of Electrical & Computer Engineering of the Hellenic Mediterranean University (HMU), Crete, Hellas. Since 2013 he is with the Electrical Machines Laboratory of the DECE, DUTH. His research interests include electrical machines design, analysis, modeling, optimization and control as well as AI methods application to the above areas. He has published several papers in various international journals and conferences as well as book chapters in international engineering books. He has participated in research projects as a research leader or scientific associate. He serves as an Associate Editor and as an Editorial board member in various international scientific journals. Prof. Karnavas is a Chartered electrical engineer as well as a member of Hellenic Technical Chamber. He is also a senior member of IEEE and member of IEEE Power Engineering Society (PES), IEEE Industry Applications Society (IAS) and IEEE Industrial Electronics Society (IES).

ORCID

Yannis L. Karnavas  <http://orcid.org/0000-0002-7390-3249>

References

- [1] Chasiotis ID, Karnavas YL. Design, optimization and modelling of high power density direct-drive wheel motor for light hybrid electric vehicles. In Donato T, editor. Hybrid electric vehicles. InTech; 2017. ISBN 978-953-51-3297-4, 158 pages. DOI: [10.5772/intechopen.68455](https://doi.org/10.5772/intechopen.68455)

- [2] Pellegrino G, Vagati A, Boazzo B, et al. Comparison of induction and pm synchronous motor drives for EV application including design examples. *IEEE Trans Ind Appl.* **2012**;48(6):2322–2332. DOI:10.1109/TIA.2012.2227092
- [3] Pellegrino G, Vagati A, Guglielmi P, et al. Performance comparison between surface-mounted and interior pm motor drives for electric vehicle application. *IEEE Trans Ind Electron.* **2012**;59(2):803–811. DOI:10.1109/TIE.2011.2151825P
- [4] Dong J, Huang Y, Jin L. Comparative study of surface-mounted and interior permanent-magnet motors for high-speed applications. *IEEE Trans Appl Supercond.* **2016**;26(4):1–4. DOI:10.1109/TASC.2016.2514342
- [5] Wang J, Yuan X, Atallah K. Design optimization of a surface-mounted permanent-magnet motor with concentrated windings for electric vehicle applications. *IEEE Trans Vehicular Technol.* **2013**;62(3):1053–1064. DOI:10.1109/TVT.2012.2227867
- [6] Gieras JF. Permanent magnet motor technology-design and applications. 3rd ed., New York: Taylor and Francis Group; **2008**. ISBN 9781420064407
- [7] Jiang X, Huang W, Cao R, et al. Electric drive system of dual-winding fault-tolerant permanent magnet motor for aerospace applications. *IEEE Trans Ind Electron.* **2015**;62(12):7322–7330. DOI:10.1109/TIE.2015.2454483
- [8] Karnavas YL, Chasiotis ID, Korkas CD, et al. Modelling and multiobjective optimization analysis of a permanent magnet synchronous motor design. *Int J Numer Model Electron Net Devices Fields.* **2017**;30(6):e2232. DOI:10.1002/jnm.2232
- [9] Hlioui S, Nedjar B, Vido L, et al. 2D-3D magnetic equivalent circuit of the flux focusing permanent magnets synchronous machine. *International Conference on Electrical Sciences and Technologies in Maghreb (CISTEM)*, Nov. 3–6. 2014. DOI:10.1109/CISTEM.2014.7077007.
- [10] Ding W, Yin Z, Liu L, et al. Magnetic circuit model and finite-element analysis of a modular switched reluctance machine with e-core stators and multi-layer common rotors. *IET Electric Power Appl.* **2014**;8(8):296–309. DOI:10.1049/iet-epa.2013.0366
- [11] Wojciechowski RM, Jedryczka C, Demenko A, et al. Strategies for two-dimensional and three-dimensional field computation in the design of permanent magnet motors. *IET Sci Meas Technol.* **2015**;9(2):224–233. DOI:10.1049/iet-smt.2014.0189
- [12] Nair SS, Chen L, Wang J, et al. Computationally efficient 3D analytical magnet loss prediction in surface mounted permanent magnet machines. *IET Electric Power Appl.* **2017**;11(1):9–18. DOI:10.1049/iet-epa.2016.0079
- [13] Alhamadi MA, Demerdash NA. Modeling and experimental verification of the performance of a skew mounted permanent magnet brushless DC motor drive with parameters computed from 3D-FE magnetic field solutions. *IEEE Trans Energy Conver.* **1994**;9(1):26–35. DOI:10.1109/60.282473
- [14] Mollet Y, Gyselinck J, Sabariego RV. Influence of 2D and 3D meshes in FE computation of eddy-current losses in surface PMSMs. *Optimization of Electrical and Electronic Equipment (OPTIM) & Intl. Aegean Conference on Electrical Machines and Power Electronics (ACEMP)*. 2017 May 25–27; Brasov. DOI:10.1109/OPTIM.2017.7975009.
- [15] Okitsu T, Matsuhashi D, Gao Y, et al. Coupled 2-D and 3-D eddy current analyses for evaluating eddy current loss of a permanent magnet in surface PM motors. *IEEE Trans Magn.* **2012**;48(11):3100–3103. DOI:10.1109/TMAG.2012.2197189
- [16] Keranen J, Ponomarev P, Pippuri J, et al. Parallel performance of multi-slice method for skewed electrical machines. *IEEE Conference on Electromagnetic Field Computation (CEFC)*. 2016 Nov 13–16; Miami, FL. DOI:10.1109/CEFC.2016.7815921.
- [17] Ponomarev P, Keranen J, Lyly M, et al. Multi-slice 2.5D modelling and validation of skewed electrical machines using open-source tools. *IEEE Conference on Electromagnetic Field Computation (CEFC)*. 2016 Nov 13–16. Miami, FL. DOI:10.1109/CEFC.2016.7815918.
- [18] Yahiaoui A, Bouillault F. 2D and 3D numerical computation of electrical parameters of an induction motor. *IEEE Trans Magn.* **1994**;30(5):3690–3692. DOI:10.1109/20.312742
- [19] Yamazaki K. Modification of 2D nonlinear time-stepping analysis by limited 3D analysis for induction machines. *IEEE Trans Magn.* **1997**;23(2):1694–1697. DOI:10.1109/20.582598

- [20] Yamazaki K. Induction motor analysis considering both harmonics and end effects using combination of 2D and 3D finite element method. *IEEE Trans Energy Convers.* **1999**;4(3):698–703. DOI:10.1109/60.790938
- [21] Dziwniel P, Piriou F, Ducreux JP, et al. A time-stepped 2D-3D finite element method for induction motors with skewed slots modeling. *IEEE Trans Magn.* **1999**;35(3):1262–1265. DOI:10.1109/20.767180
- [22] Dalcali A, Akbaba M. Comparison of 2D and 3D magnetic field analysis of single-phase shaded pole induction motors. *Engin Sci Technol Int J.* **2016**;19(1):1–7. DOI:10.1016/j.jestch.2015.04.013
- [23] Bianchi N, Bolognani S. Design techniques for reducing the cogging torque in surface-mounted PM motors. *IEEE Trans Ind Appl.* **2002**;38(5):1259–1265. DOI:10.1109/TIA.2002.802989
- [24] Ebrahimi BM, Faiz J. Magnetic field and vibration monitoring in permanent magnet synchronous motors under eccentricity fault. *IET Electric Power Appl.* **2012**;6(1):35–45. DOI:10.1049/iet-epa.2010.0159
- [25] Woo DK, Lim DK, Yeo HK, et al. A 2-D finite-element analysis for a permanent magnet synchronous motor taking an overhang effect into consideration. *IEEE Trans Magn.* **2013**;49(8):4894–4899. DOI:10.1109/TMAG.2013.2248374
- [26] Cetin E, Daldaban F. Analyzing distinctive rotor poles of the axial flux PM motors by using 3D-FEA in view of the magnetic equivalent circuit. *Engin Sci Technol Int J.* **2017**;20(5):1421–1429. DOI:10.4186/ej.2017.21.1.193
- [27] Karnavas YL, Chasiotis ID. Influence of soft magnetic materials application to squirrel cage induction motor design and performance. *Eng J.* **2017**;21(1):193–206. DOI:10.4186/ej.2017.21.1.193
- [28] Arkkio A. Finite element analysis of cage induction motors fed by static frequency converters. *IEEE Trans Magn.* **1990**;26(2):551–554. DOI:10.1109/20.106376
- [29] Paula GT, Monteiro JRA, Alvarenga BP, et al. On-load back emf of PMSM using Maxwell stress tensor. *IEEE Trans Magn.* **2018**;54(7):1–15. DOI:10.1109/TMAG.2018.2829692